>*Int. J. Electrochem. Sci.*, 15 **(2020)** 12654 – 12670, doi: 10.20964/2020.12.69

International Journal of
ELECTROCHEMICAL
SCIENCE
www.electrochemsci.org

A Computational Fluid Dynamics Study in a PEM Fuel Cell with Different Flow Fields

C. E. Hernández-Herrera, S. J. Figueroa-Ramírez, H. Mandujano, L. Santis, J. M. Sierra[*]

Facultad de Ingeniería, Universidad Autónoma del Carmen. Cd. del Carmen, Campeche 62580, México.
[*]E-mail: juanmsg@live.com.mx, jsierra@pampano.unacar.mx

Received: 3 August 2020 / *Accepted:* 19 September 2020 / *Published:* 31 October 2020

In this paper, a computational fluid dynamics (CFD) study in a proton exchange membrane fuel cell model with different flow field designs is presented. The study was carried out to investigate the effects caused by serpentine, parallel, interdigitated and spiral channel configurations on the performance of fuel cells. An active area of 24 cm2 for all flow fields was considered. From a commercial CFD code that solves governing equations and an electrochemical model, local distributions of pressure, temperature, species, proton conductivity and current density contours were obtained. The numerical results were analyzed in detail and showed the contribution of each transport phenomenon to the electrochemical reactions that take place inside of the fuel cell. The simulations were carried out with operating conditions of a pressure of 3 atm, a temperature of 353 K and a relative humidity of 100%. The numerical results demonstrated that the spiral flow field is better than the other tested designs because it homogeneously distributes the species over the entire active area of the cell, which allows a better distribution of temperature and proton conductivity in the membrane and catalyst layer, respectively, favoring mass and energy transport through the fuel cell.

Keywords: PEM; Fuel cell; CFD; Flow Field.

1. INTRODUCTION

Energy plays a fundamental role in human life, and the capacity of a society to obtain, transform and store it determines whether the energy is sufficient to satisfy the basic needs of comfort, mobility, communication and technological development. However, due to the accelerated industrialization of some countries and the population growth worldwide, the consumption of fossil fuels has increased dramatically. This demand for energy has caused a serious reduction in fossil fuel reserves and an increase in greenhouse gases in the atmosphere. Due to these situations, the governments of many countries have chosen to use other energy sources, such as renewable energy and some clean

technologies, among which fuel cells stand out. Fuel cells, particularly proton exchange membrane fuel cells (PEMFCs), are the most attractive alternative to provide power for transport and portable devices. Their high efficiency and low emissions have encouraged their use for supplying electricity to the new age of vehicles. The scalability and flexibility of PEMFCs make them prime candidates for a variety of portable and stationary applications. However, high material costs and the large-scale production process are some of the main challenges facing this technology. For this reason, design optimization plays an important role in reducing the manufacturing costs of fuel cells. Nevertheless, advances in the development of fuel cells require a better understanding of the transport phenomena [1,2]. The use of experimental studies alone is difficult, but with recent advances in computer systems, mathematical models are becoming more robust and accurate to calculate and predict the phenomena of mass and energy transport that occur inside of the PEM fuel cell.

The processes of heat and mass transfer are directly related to the electrochemical reactions that take place in the electrodes of a fuel cell [3]. Thus, the PEMFC performance is a function of the efficiency with which the mass transport processes are carried out, and this depends on the design of the flow field engraved on the bipolar plates.

Bipolar plates and the ribs of the flow field provide the contact surface for electron transport, and gases are supplied to the reaction sites through the channels [4]. However, there are different ways of distributing gases through flow fields or channel configurations [5,6]. The serpentine flow field is the most popular pattern used in commercial fuel cells [6], and many variations are available; some designs feature a single channel, while others have channels in parallel form [7-9]. Additionally, some researchers have proposed new fuel cell designs to improve the flow distribution evenly and reduce pressure gradually from inlet to outlet [10].

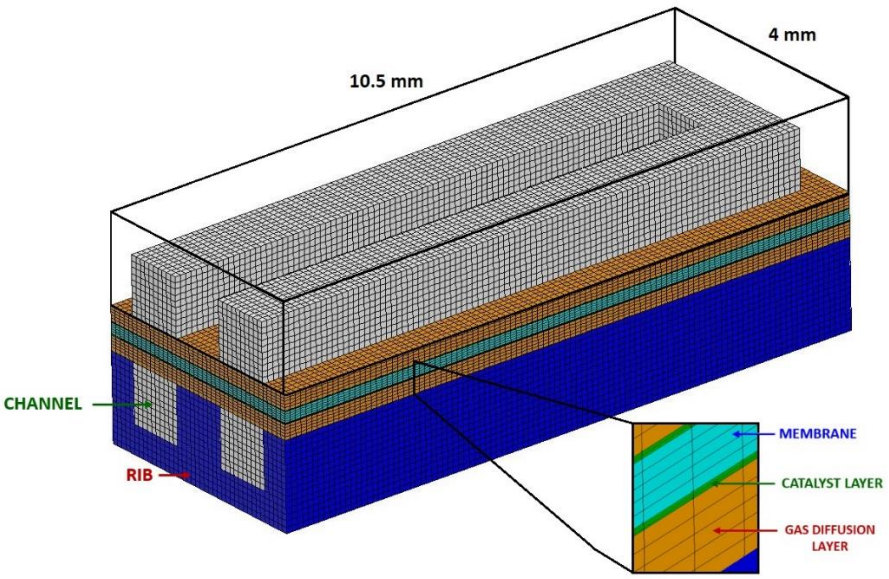

Figure 1. Schematic representation of the base model, mesh and components of the PEM fuel cell.

Unlike other investigations reported in the literature [4, 6, 8, 10], this study is focused on the detailed description of the mass transport at the interfaces of both electrodes considering four basic designs of flow fields. Likewise, before carrying out the simulations of the four flow field models, a base model was developed and evaluated to validate the results with data reported in the literature. The base model consisted of a section of a serpentine channel with one turn, as shown in Fig. 1.

The models were evaluated under the following conditions; the reactant gases were simultaneously injected into the fuel cell models according to previous studies [11]. The active area of the flow field considered for the models was approximately 24 cm^2. The relationship between the dimensions of the canal and the rib was 50/50. A channel width and height of 1 x 1 mm were considered. The geometric characteristics of the models are shown in Fig. 2 and Table 1.

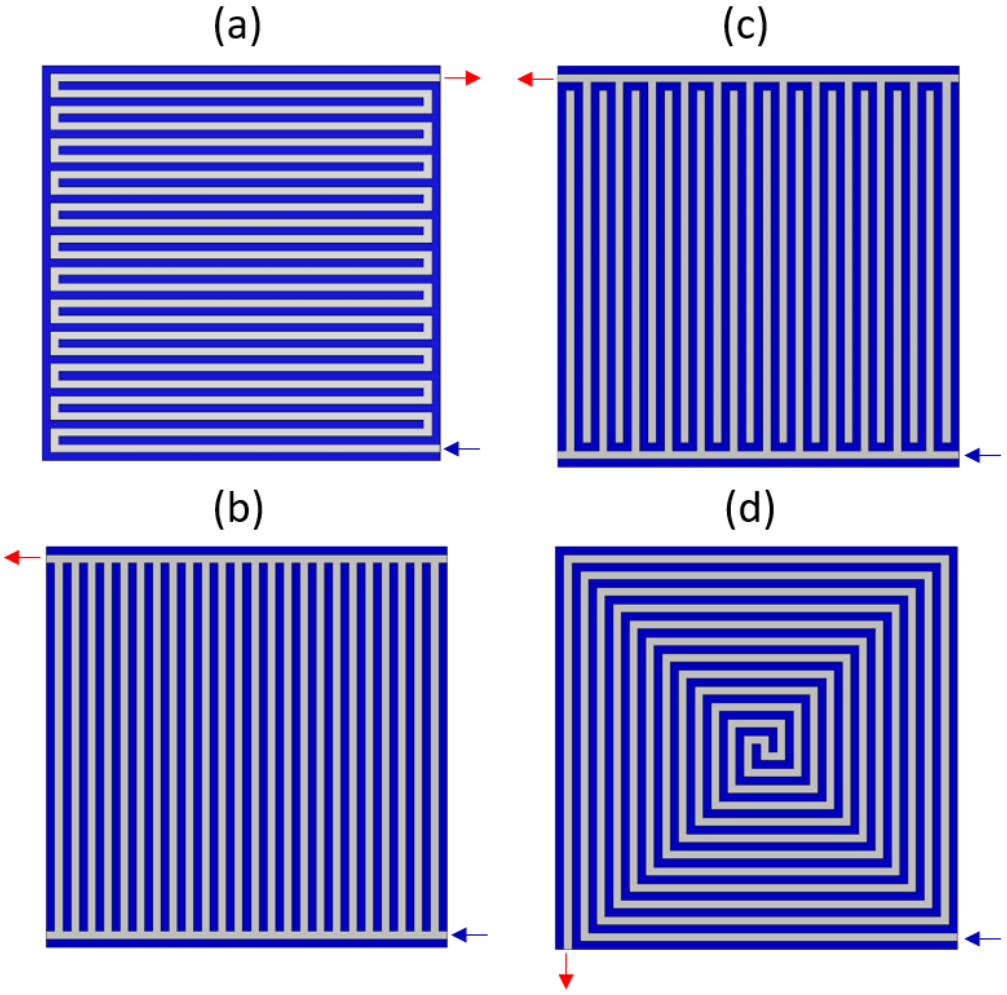

Figure 2. Geometry of different flow field designs. a) Serpentine, b) parallel, c) interdigitated and d) spiral.

2. MODEL DEVELOPMENT

The computational models evaluated in this work consist of an individual fuel cell with single channels, gas diffusion layers (GDLs), catalyst layers (CLs), membranes (MEMs) and monopolar plates (MPs). The model was built in CAD software. The geometry and dimensions of the domain of the PEMFC are shown in Fig. 2 and Table 1, respectively.

Table 1. Model dimensions

Channel height	mm	1.0
Channel width	mm	1.0
Rib width	mm	1.0
Rib height	mm	1.0
Cell active area	mm^2	2401
Gas diffusion layer thickness	mm	0.25
Catalyst layer thickness	mm	0.02
Membrane thickness	mm	0.178

2.1 Model asssumptions

To solve the computational domain, the following assumptions were considered: (i) the fuel cell operates under steady-state conditions; (ii) based on the Reynolds number calculation, a laminar flow was considered in the channels; (iii) there are isotropic porous zones; (iv) liquid water, energy and protons are transported in the membrane; (v) electrochemical reactions take place on the surface of both electrodes; (vi) the reacting species are balanced electrochemically by the production/consumption rate, according to the half-cell reactions; (vii) the model includes the gas species transport, proton transport, energy transport and diluted water in the membrane; and (viii) the transport of liquid water in the membrane is controlled by diffusion mechanisms and electro-osmotic drag.

To ensure the accuracy and validity of the results and to reduce the CPU time, an independent grid study was performed. The mesh type used in the models was the same as that used for the base model (Fig. 1), but the number of elements in the designs was approximately 4.2 million for each one. A grid size of 0.25 for ribs and channels, 0.05 for GDLs, 0.004 for CLs, and 0.035 for MEMs was used.

2.2 Mathematical model

The mathematical model used in this work is the same as that described in a previous work by the authors [13]. This model consists of the basic equations of computational fluid dynamics, an electrochemical model to solve the potential fields and the general Butler-Vomer formulation to calculate the current density in the catalyst layers.

2.3 Operating and boundary conditions

Operating conditions such as 3 atm of pressure, 353 K of temperature and a relative humidity of 100% were considered in the cell and flows to obtain an adequate level of membrane hydration. Both electrochemical parameters and porous media properties have been discussed in previous works by the authors [12, 13]. The parameters and boundary conditions used to carry out the simulation are presented in Table 2.

Table 2. Physical and electrochemical parameters

Pressure	P_{an}	atm.	3
Temperature (H_2, O_2)	T_i	K	353
Relative humidity (H_2, O_2)	-	%	100
Ref. exchange current density. (an)	j_{an}^{ref}	$A.m^{-3}$	1.5×10^9
Ref. exchange current density. (cat)	j_{cat}^{ref}	$A.m^{-3}$	4×10^6
Anode transfer coefficient	α_{an}	-	2
Cathode transfer coefficient	α_{cat}	-	2
Concentration exponent (an)	γ_{an}	-	0.5
Concentration exponent (cat)	γ_{cat}	-	1
GDL porosity	ϵ_{GDL}	-	0.4
GDL viscous resistance	$v_{R,GDL}$	-	1×10^{12}
CL porosity	ϵ_{CL}	-	0.2
CL Viscous resistance	$v_{R,CL}$	-	4×10^{12}

3. RESULTS AND DISCUSSION

The numerical results obtained by the simulation are presented in this section. These results are divided by the type of flow field; the contours for the anode side are discussed first, and then those for the cathode side are discussed. These results are analyzed in detail at the interfaces of the catalyst layer/gas diffusion layer, as well as the membrane/catalyst layer interface and cathode plate.

Likewise, the results shown below are reported at a potential of 0.2 V, among which the effects of each flow field presented the greatest differences in the polarization curves.

3.1 Serpentine Design

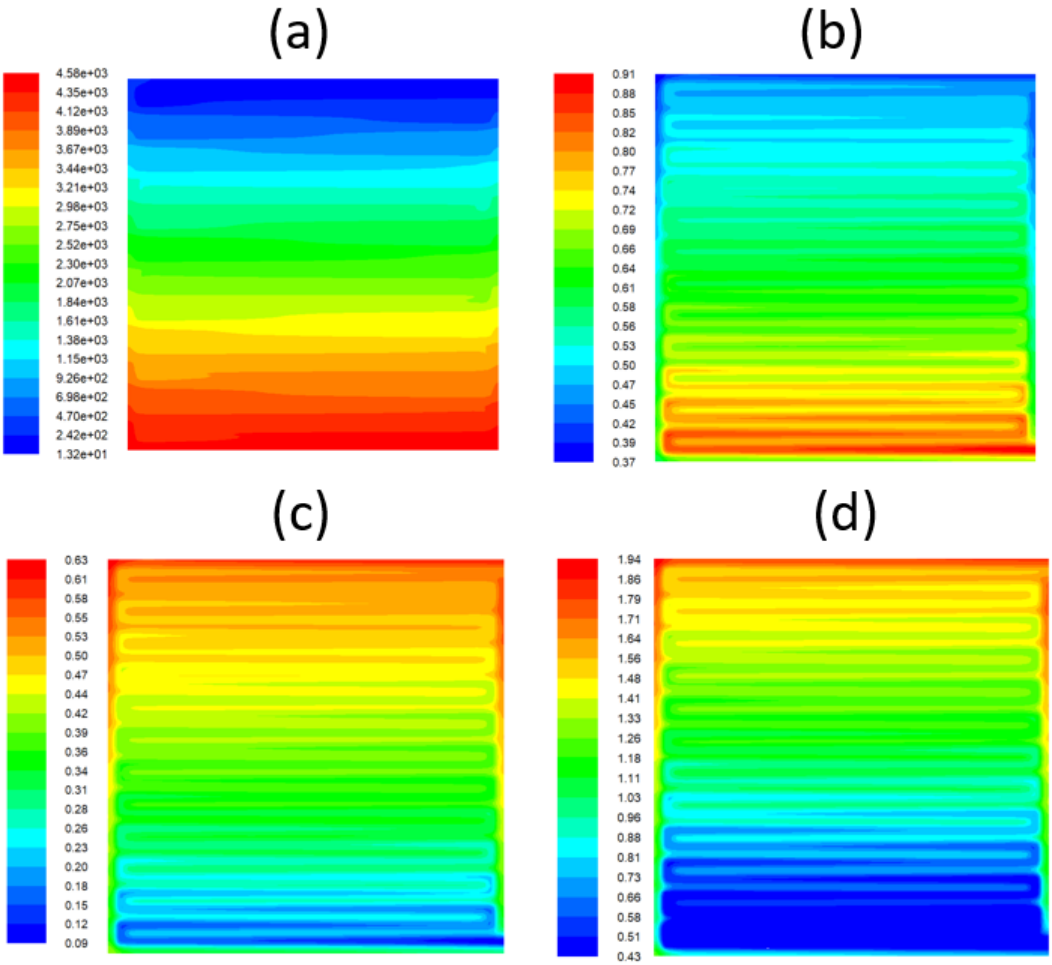

Figure 3. Contours for the serpentine design (anode): (a) static pressure (Pa), (b) hydrogen mass fraction, (c) water mass fraction and (d) proton conductivity (ohm^{-1} m^{-1}).

In Fig. 3, the simulation results for the serpentine design are presented. Figure 3(a) shows the pressure losses at the anode (GDL/CL) interface, where the pressure of the hydrogen/water vapor mixture at the inlet was 4,580 Pa. This pressure drop increases along the flow field due to the length of the channel and the characteristic turns of this design. In this way, the gas travels through the entire flow field until it reaches the outlet with a pressure of 13.2 Pa. b) The hydrogen concentration is approximately 0.91 at the inlet and decreases to 0.37 at the gas outlet. In Fig. 3(c), the water concentration is 0.09 at the

inlet, and its concentration increases until water reaches the area located near the outlet (0.63). This happens because hydrogen is consumed from the beginning of the flow field by reaction in the catalyst layer. The highest proton conductivity values are found in (d), where the water concentration is highest and vice versa. It is evident that the proton conductivity of this side of the membrane is directly related to the concentration of water at the anode.

On the other hand, some distribution patterns similar to the anode side occur on the cathode side for the serpentine design, as observed in Fig. 4. In (a), the pressure distribution at the GDL/CL interface is high at the inlet (5,470 Pa) and low at the outlet (- 26 Pa). The pressure increase for this side of the cathode is slightly higher than at the anode, mainly due to the mass transport processes related to the properties of the oxygen/water mixture. In (b), the oxygen concentration is high at the first half of the GDL/CL interface. However, due to the oxygen consumption of the electrochemical reaction of this side of the cell, its concentration decreases considerably along the serpentine channel.

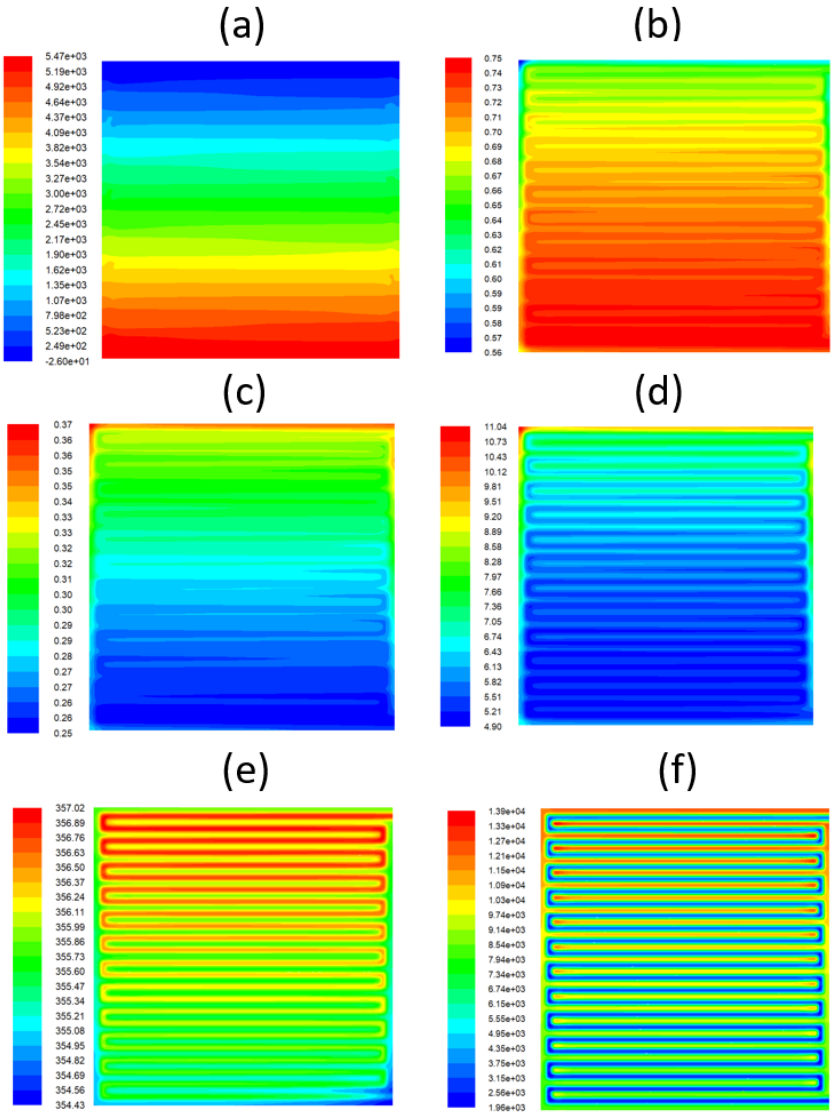

Figure 4. Contours for the serpentine design (cathode): (a) static pressure (Pa), (b) oxygen mass fraction, (c) water mass fraction, (d) proton conductivity (ohm^{-1} m^{-1}), (e) temperature (K) and (f) current density (A/m^2).

In (c), the behavior of the water distribution is opposite to that of oxygen; in this case, the water generation on this side of the cathode contributes to an increase in the amount of downstream water near the outlet. Figure (d) shows the proton conductivity at the CL/MEM interface of the cathode, and as in the case of the description of the anode, this parameter is related to the distribution of water concentration in this interface. In (e), the temperature distribution is shown, which has high values in the flow channels and low values in the ribs. Likewise, it is observed that the temperature gradually increases from the first third in this interface to increase by 3.6 K above the inlet temperature of 353 K. This occurs by the heat drag transported by the fluid and the heat generated by the electrochemical reactions that take place in the cathode. In (f), the contours of the current density distribution in the outer wall of the plate are presented. This figure shows that the highest density intensity comes from the ribs of the flow field, and the highest values occur in the region where a greater water content and a high proton conductivity exist.

3.2 Parallel Channel Design

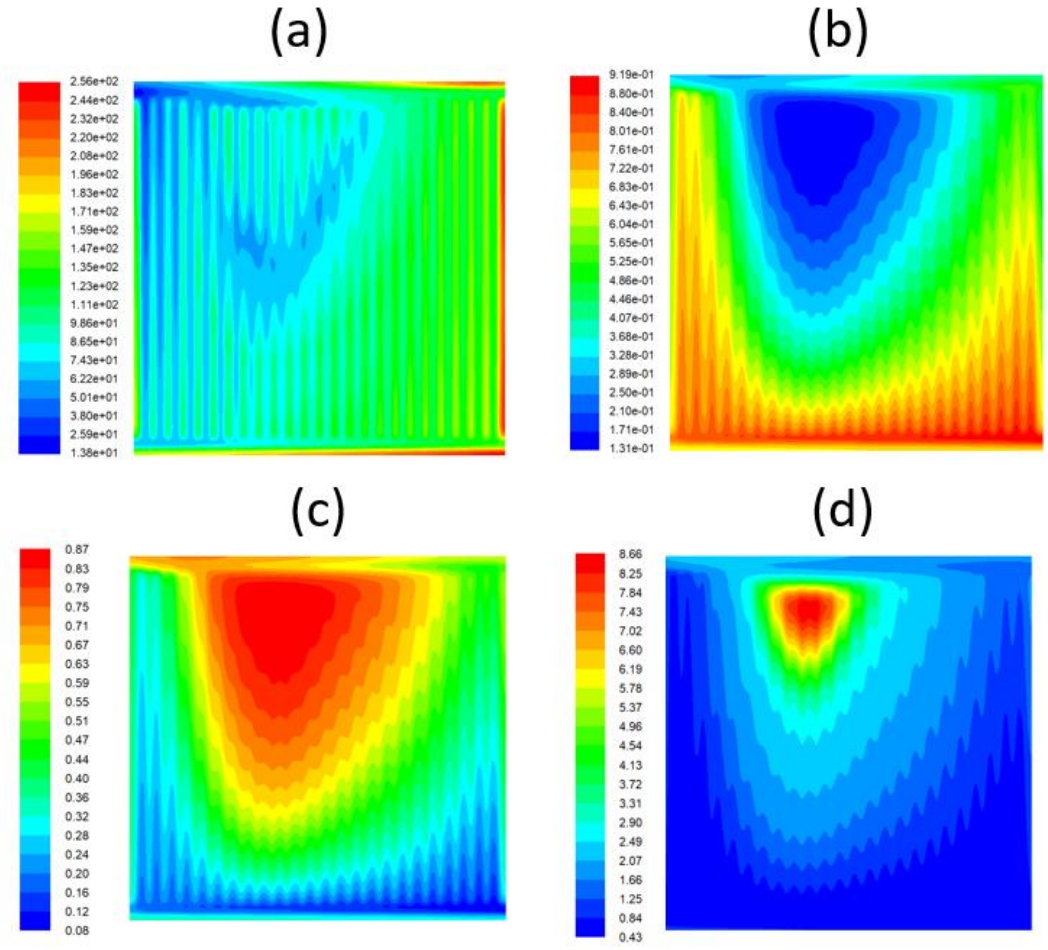

Figure 5. Contours for the parallel channel design (anode): (a) static pressure (Pa), (b) hydrogen mass fraction, (c) water mass fraction and (d) proton conductivity (ohm^{-1} m^{-1}).

The simulation results for the parallel channel design are presented in Fig. 5. The pressure distribution in (a) is relatively high only in the first half of the GDL/CL interface; the highest value was 256 Pa and decreases to the outlet with a value of 13.8 Pa). This design featured the lowest pressure

drops. The hydrogen concentration shown in (b) was high at the main inlet channel, as well as in the first and last perpendicular channels, and the gas concentration decreased in the center of the catalyst layer to 0.13, which was the lowest value of all the models. In (c), the concentration of water is opposite to that of oxygen, with a high value (0.97) in the center of the CL until reaching the main outlet channel (0.08). In this design, the water cannot be efficiently expelled from the flow field. d) The highest proton conductivity values are found where the water concentration is highest and vice versa. It is evident that the proton conductivity on this side of the membrane is directly related to the concentration of water at the anode.

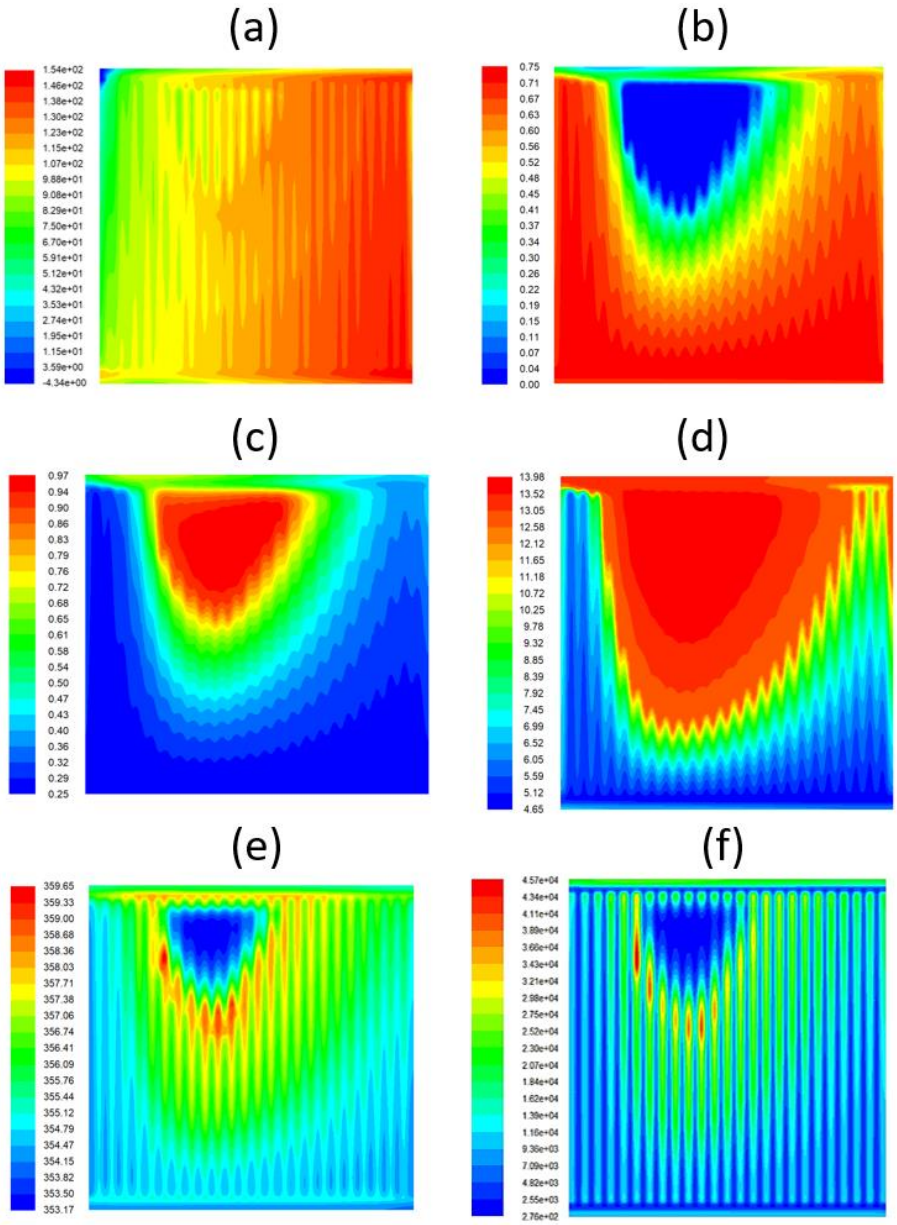

Figure 6. Contours for the parallel channel design (cathode): (a) static pressure (Pa), (b) oxygen mass fraction, (c) water mass fraction, (d) proton conductivity (ohm^{-1} m^{-1}), (e) temperature (K) and (f) current density (A/m^2).

The results for the cathode of the flow field with parallel channels are shown in Fig. 6. In (a), the pressure is high at the first half of the GDL/CL interface with a value of approximately 154 Pa and is gradually reduced in the other half of the interface until it reaches the outlet, with a value of -4.34 Pa. In (b), high concentrations are observed in two-thirds of the active area, which depends on the shape of the channels. In (c), it is observed that water cannot be easily removed in the area near the center and the gas outlet. Figure (d) shows that the proton conductivity for the parallel flow field is higher than that for the other designs. The impact of water concentration is most noticeable for this flow field. In (e), the temperature distribution is shown, and the highest values (359.65 K) are presented where the highest concentrations of water converge for both the anode and the cathode. This can be attributed to the heat generated by the electrochemical reactions and the high ion transport that occurs on both sides of the membrane. In (f), the current density distribution contours are shown. The distribution pattern is similar to the proton conductivity at the CL/MEM interface; however, the lack of oxygen in the central region near the main outlet channel is observed.

3.3 Interdigitated Design

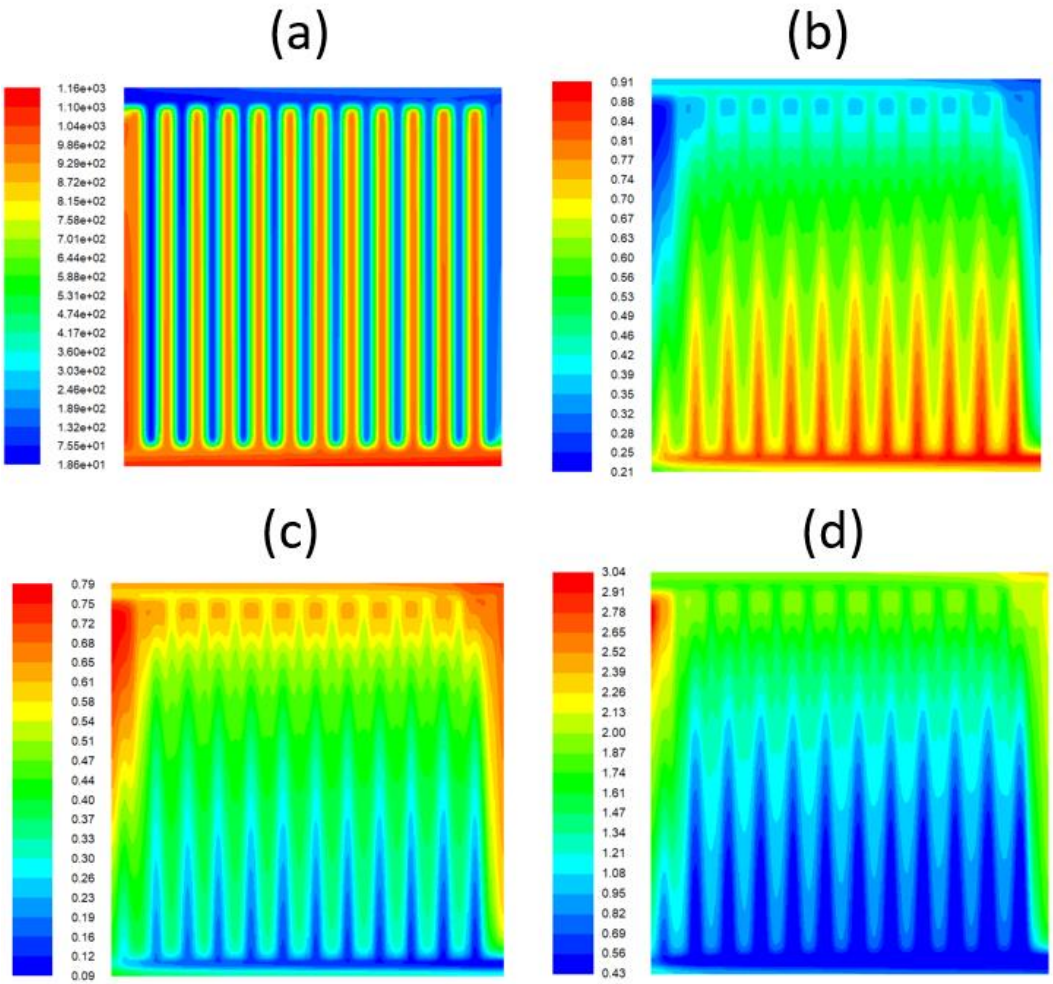

Figure 7. Contours for the interdigitated design (anode): (a) static pressure (Pa), (b) hydrogen mass fraction, (c) water mass fraction and (d) proton conductivity (ohm^{-1} m^{-1}).

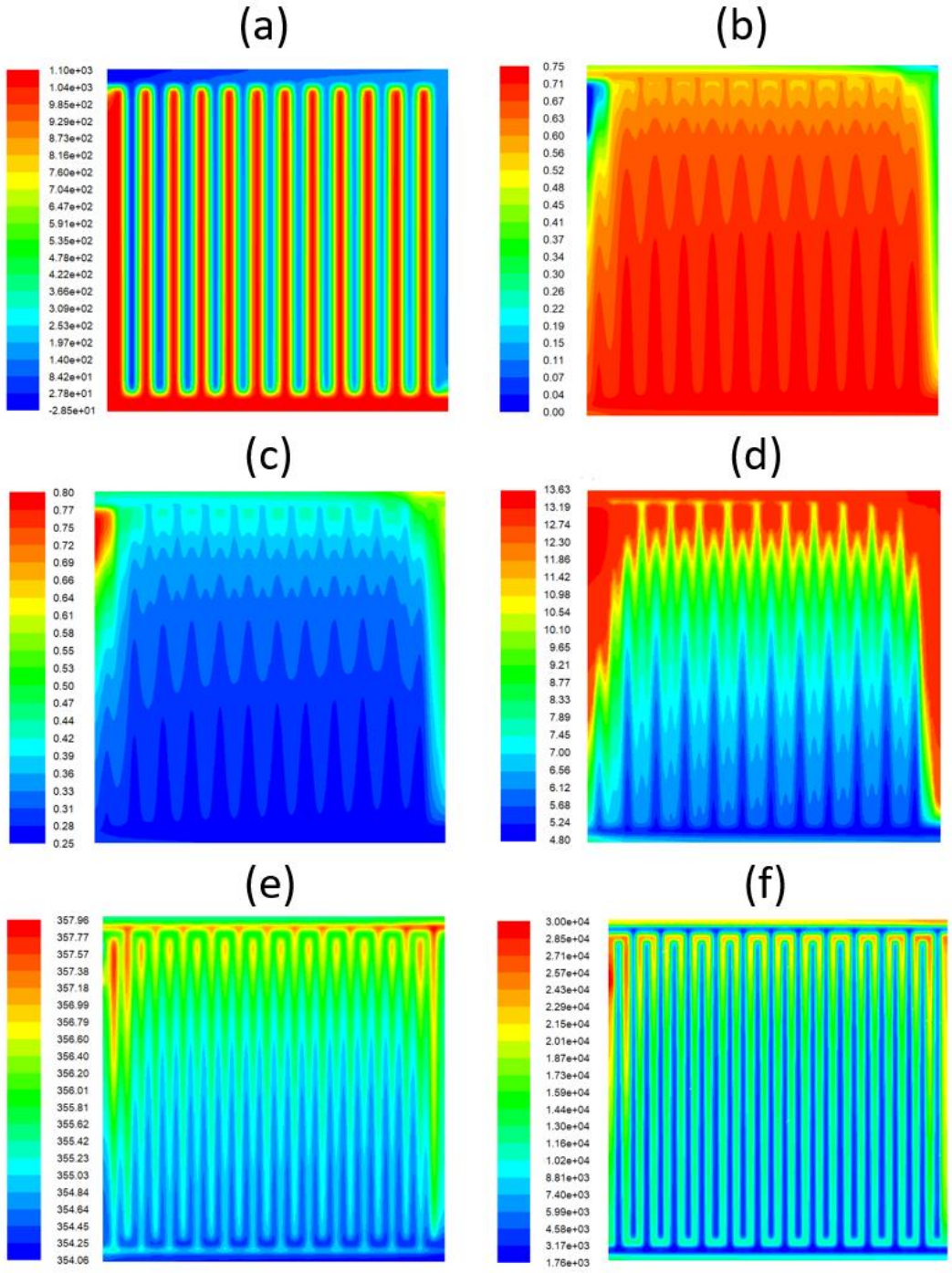

Figure 8. Contours for the interdigitated design (cathode): (a) static pressure (Pa), (b) oxygen mass fraction, (c) water mass fraction, (d) protonic conductivity (ohm^{-1} m^{-1}), (e) temperature (K) and (f) current density (A/m^2).

The results for the interdigitated flow field are presented in Fig. 7. In (a), it is observed that the pressure in the inlet channels is high (1,160 Pa); this happens because the flow field is not continuous. The first section corresponds to a flow field that supplies the gas, which rises to the gas diffusion layer and is dispersed; then, both by diffusion and by pressure differences, it leaves through the GDL and via the second section of the flow field, thus being evacuated. This process is clearly seen in (a). In (b), it is

observed that the hydrogen concentration is high in the region of the supply flow field (0.91) and is gradually reduced from the entrance to the region located near the exit of the other flow field (0.21). In the case of water (c), its distribution is the opposite, as in all cases; however, it is observed that this flow field drags the water to the outlet channel. In Figure 7(d), the proton conductivity presents a distribution pattern similar to the water concentration.

The results for the cathode are shown in Fig. 8. In (a), the pressure distribution exhibits a behavior similar to that on the anode side, but in this case, the pressure values are lower. In (b), the oxygen concentration is high in both the main inlet channel and in the perpendicular channels. In (c), the water is effectively removed from the flow field. Figure (d) shows that the highest conductivity values are found in the zones where this flow field removes excess water. In (e), it is observed that the temperature distribution and its highest values (357 K) are related to the protonic conductivity and the water concentration. In (f), it is observed that the current density distribution and the highest values coincide with the ribs of the flow field and where the highest values of protonic conductivity are presented (<12); however, in this case, the absence of oxygen does not affect the current density.

3.4 Spiral Design

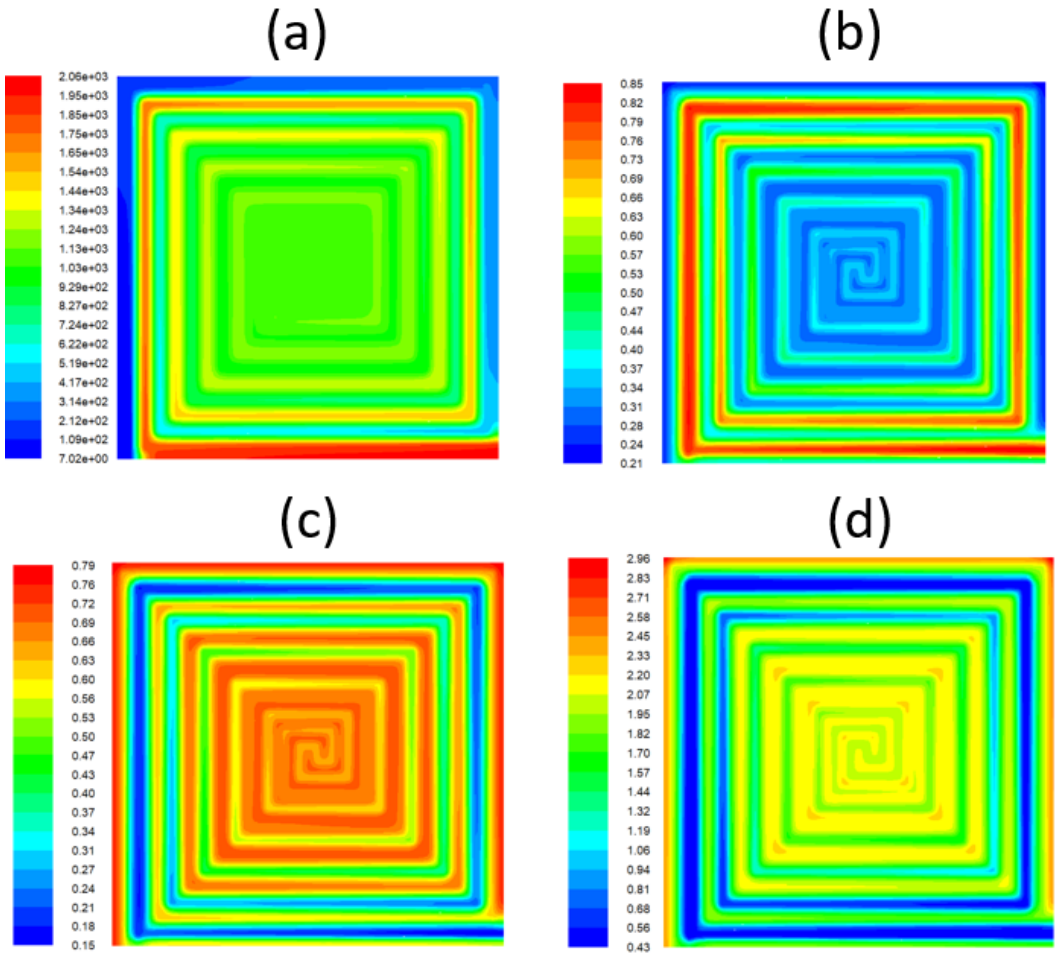

Figure 9. Contours for the spiral design at the GDL/CL interface (anode): (a) static pressure in Pa, (b) hydrogen mass fraction, (c) water mass fraction and (d) protonic conductivity (ohm^{-1} m^{-1})

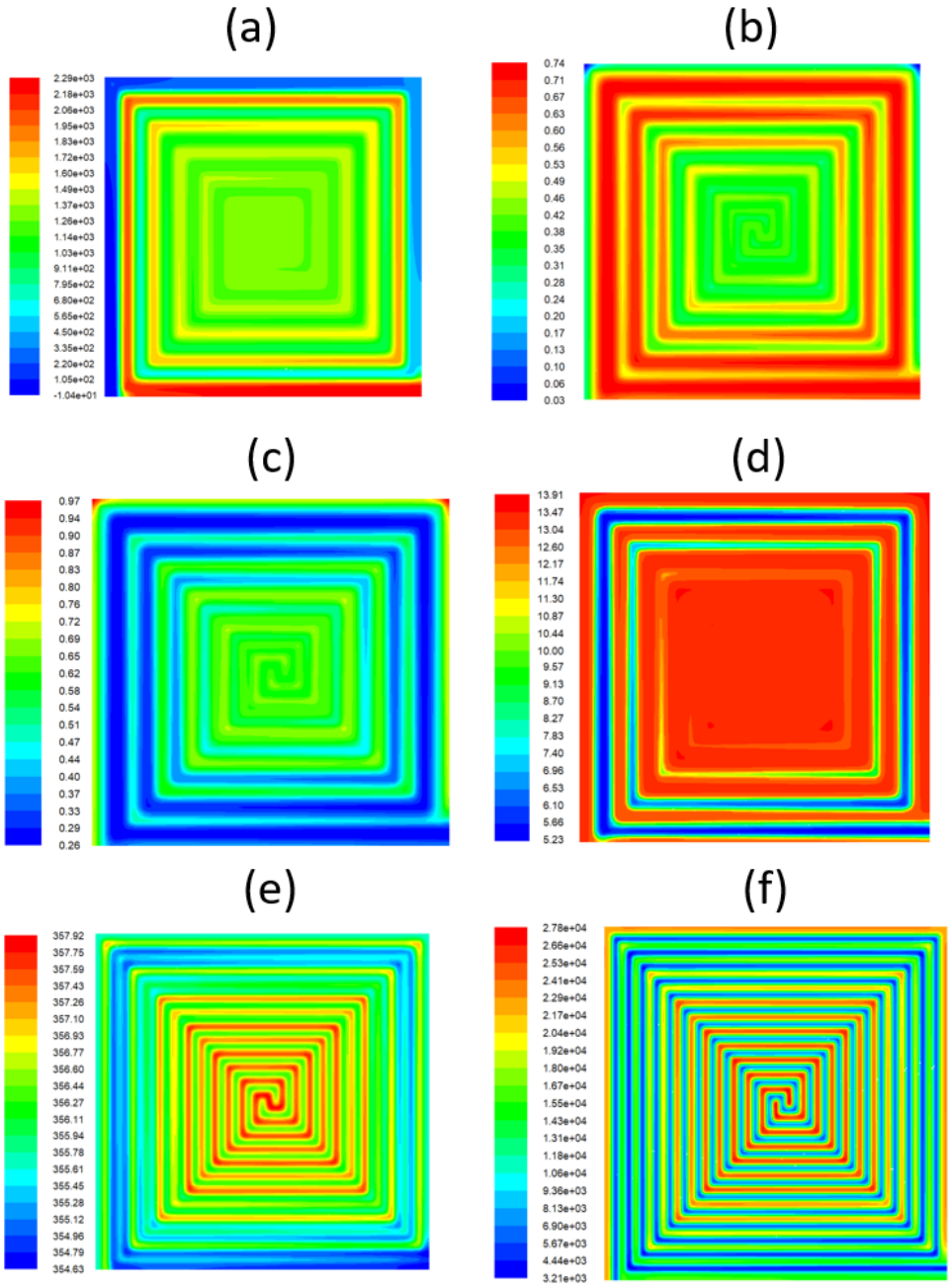

Figure 10. Contours for the interdigitated design (cathode): (a) static pressure (Pa), (b) oxygen mass fraction, (c) water mass fraction, (d) protonic conductivity at the CL/MEM interface (ohm^{-1} m^{-1}), (e) temperature (K) and (f) current density (A/m^2).

In Fig. 9, the results for the spiral design are presented. For this flow field, (a) the pressure drop at the interface (GDL/CL) is observed from the inlet with a value of 2,060 Pa to 7.02 Pa at the outlet. In (b), the hydrogen concentration for this design presents the same behavior as the other flow fields, with high concentrations at the inlet, and low concentrations at the outlet; however, it is evident that in the center of the flow field, the hydrogen concentration is lower. Unlike the other designs and due to the geometry of the flow field itself, this design causes water accumulation in the center of the cell (c).

Finally, in (d), the protonic conductivity for the spiral design was the most uniform over the entire active area of the membrane.

The results for the spiral flow field on the cathode side are presented in Fig. 10. In (a), the same distribution patterns are observed as the other designs. In (b), the oxygen concentration is uniform in a large part of the active area. In (c), the water concentration is only homogeneous in the center of the cell. In (d), it is observed that this design showed the most uniform proton conductivity distributions over the entire membrane. In (e), the temperature distribution showed high values (357 K) in the channels due to the electrochemical reaction of oxygen on the catalyst layer. In (f), the contours of the current density distribution showed greater intensity in the center of the cell due to the factors described above. A similar pattern of current density distribution was also reported by Juarez [14].

In summary, the flow fields that showed a more even gas distribution over the active area of the fuel cell were the spiral design and the parallel channel design. Both designs allow better utilization of the reactant gases supplied to the cell. The serpentine flow field presented the highest pressure drops, as was also reported by Weng [15].

The hydrogen and oxygen concentrations in all designs were always high at the inlet and gradually reduced along the channel to the outlet. Flow fields that showed a higher concentration of reactant gases in the active area were the serpentine and interdigitated designs, and the other flow fields showed a reduction in the concentration of gases at the outlet and the center of the cell. In contrast, the water concentration always showed an opposite distribution to the concentration of the reactant gases, and the highest concentrations were always shown at the center and outlet. In this regard, protonic conductivity on both sides of the membrane always showed a direct relationship with the concentration of water, mainly with the cathode side.

For the temperature distribution, the highest values were presented at the CL/GDL interface of the cathode; this is consistent with investigations conducted by Rahgoshay [16]. The temperature increases from 353 K to 358 K. The flow field with parallel channels showed the highest temperature. Similarly, the highest temperatures in this interface were manifested in the flow channels, and the lowest were in the ribs. The heat generated by the electrochemical reaction in the cathode contributes most to the increase in the temperature in the cell. Finally, the highest current densities occurred in the monopolar plates, and the highest values were observed with the same pattern of distribution of the flow field and over the ribs.

3.5 Polarization curves

The results obtained from the base model (Fig. 11) were validated with the experimental data reported by Siegel [17], and this comparison showed a good approximation. From the validation of these results, the authors proceeded to develop and simulate the models with different flow fields.

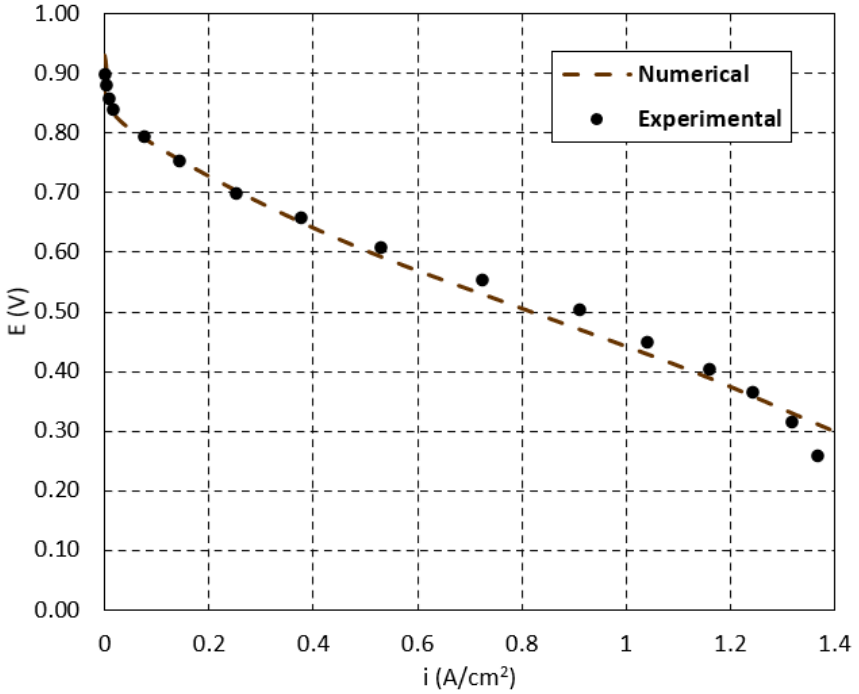

Figure 11. Comparison of the base model with the data reported in the literature (Siegel) [17].

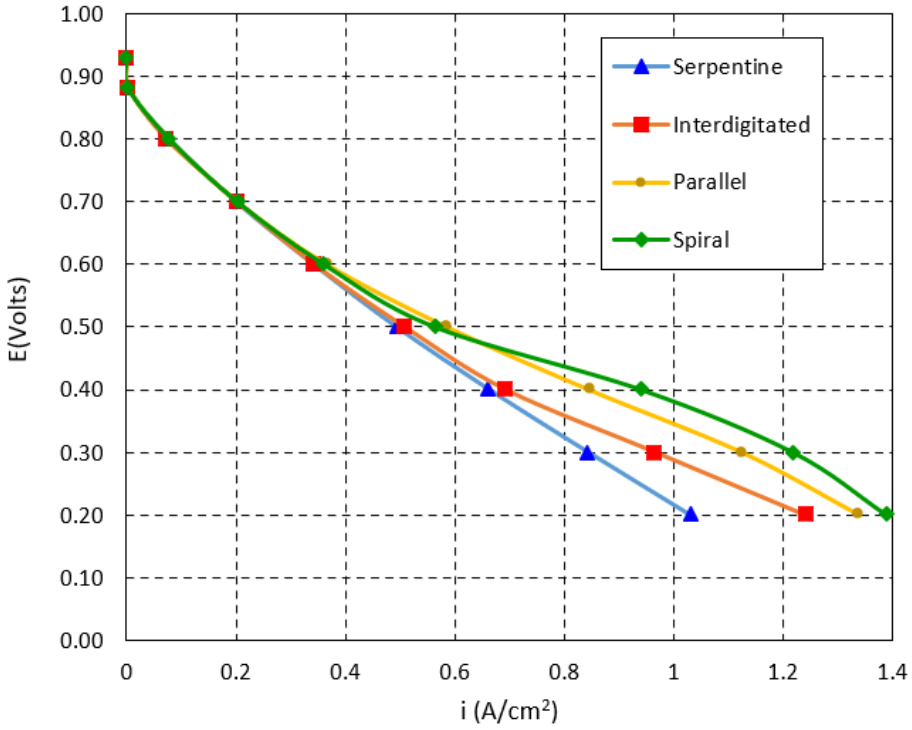

Figure 12. Numerical polarization curves for different flow fields.

The polarization curves obtained for the four flow field designs evaluated in this work are presented in Fig. 12. The maximum current density for the I-V plots was obtained at 0.2 V. Similar values were also obtained by Choi [18] for a serpentine multichannel flow field with 25 cm^2 of active area. At low potentials, mass transport losses are dominant, and the numerical solutions begin to

oscillate, making convergence difficult when potentials are even lower. The flow field that showed the best performance was the spiral design, followed by the flow fields with parallel channels, the interdigitated flow field and, finally, the design with the serpentine channel. In this way, the impact of the flow field design on the performance of a single fuel cell is demonstrated from the polarization curves.

4. CONCLUSIONS

A numerical study of computational fluid dynamics in a PEM fuel cell with different flow fields was carried out. The results demonstrated the advantages and disadvantages of each design in terms of the distribution of parameters at the different interfaces of the fuel cell. The different types of flow fields substantially influence the pressure distribution of the reactant gases in the gas diffusion layers, and the pressure is related to the concentration gradients of hydrogen and oxygen on the catalyst layer. The water concentration always has an opposite distribution of the reactant gases and is directly related to the protonic conductivity of the membrane; the concentration of water in the cathode is dominant. The highest temperature values occur in the regions of the flow channel and are always higher in the cathode than anode due to the exothermic reaction in this electrode. The contours of the current density distribution adopt the shape of the flow field. Moreover, from this study, it was shown that energy and mass transfer processes that take place in both electrodes demonstrate a similar distribution pattern in terms of pressure and species distribution; however, the hydrogen, oxygen and water concentration gradients are larger at the anode than at the cathode. In contrast, the magnitude of the concentration of water in the cathode is always greater due to the reaction that takes place on this electrode. This difference in water concentration impacts the global water content in the membrane and, in turn, the ionic conductivity, leaving dead zones in certain areas of the active area and, on the other hand, zones with excess water. This analysis demonstrates that current density distributions are directly related to the ionic conductivity of the membrane and that this is correlated with species distributions at interfaces. Finally, the polarization curves showed that the spiral flow field has the best performance among the tested designs. The shape of the channel allows the gases to be distributed homogeneously over the catalyst layer and guarantees the utilization of the entire active area of the fuel cell.

ACKNOWLEDGMENTS

The authors gratefully acknowledge CONACyT for the financial support from project 254667 “Consolidación del Laboratorio de Energía Renovable del Sureste (LENERSE)”.

NOMENCLATURE

P	Pressure (Pa)
T	Temperature (K)
RH	Relative humidity (%)
v	Viscous resistance ($1/m^2$)

j Reference exchange current density (A/m^3)

Greek letters

α Transfer coefficient
γ Concentration exponent
ϵ Porosity

Subscripts and superscripts

an anode
ca cathode
C cell
R resistance
i species i
CL Catalyst Layer
GDL Gas Diffusion Layer

References

1. Y. Chen, L. Enearu, *J. of Appl. Mech. Eng*., 5 (2016) 1.
2. A. Mohammed, Y. Sahli, H. B. Moussa, *Fuel,* 263 (2020) 116713
3. W. Li, R. Lin, Y. Yang, *Electrochim Acta*, 302 (2019) 241.
4. Y. Yin, Y. Qin, *Int. J. Hydrogen Energy*, 19 (2018) 8048.
5. A. Torkavannejad, N. Pourmahmoud, *Int. J. Hydrogen and Fuel Cell*, 2 (2016) 99.
6. R. Roshandel, *Renewable Energy*, 41 (2012) 86.
7. J. Park, X. Li, *J. of Power Sources*, 163 (2007) 853.
8. E. Alizadeh, S.H. M. Saadat, *Int. J. Hydrogen Energy*, 42 (2017) 14708.
9. D. Singdeo, P.C. Ghosh. *Appl. Energy*, 95 (2017) 13.
10. B. H. Lim, E. H. Majlan, M.I. Rosli, T. Husaini, *Int. J. Hydrogen Energy* 42 (2017) 9210.
11. J.M. Sierra, P.J. Sebastian, *J. Power Sources*, 196 (2011) 5070.
12. J. Macedo, J. M. Sierra, S. J. Figueroa, *Int. J. Hydrogen Energy*, 41 (2016) 23425.
13. J. M. Sierra, S. J. Figueroa, J. Vargas, *Int. J. Hydrogen Energy*, 39 (2014) 16694.
14. D. Juárez, A. Hernández, C. E. Damian, C. Rubio, *Proc. Int. Mech. Eng*., (2007) 42429.
15. F. B. Weng, A. Su, G.B. Jung, Y.C. Chiu, S. H. Chan, *J. Power Sources*, 145 (2005) 546.
16. S. M. Rahgoshay, A.A. Ranjbar, A. Ramiar, E. Alizadeh, *Energy,* 134 (2017) 61.
17. N. Siegel, M.W. Ellis, D. J. Nelson, M. R. von Spavosky, *J. Power Sources*, 128 (2004) 173-184.
18. K. S. Choi, *Int. J. Electrochem. Sci*., 10 (2015) 2564.